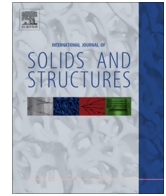




Contents lists available at ScienceDirect

International Journal of Solids and Structures

journal homepage: www.elsevier.com/locate/ijsolstr

Harnessing instability-induced pattern transformation to design tunable phononic crystals



Jongmin Shim^a, Pai Wang^b, Katia Bertoldi^{b,c,*}

^aDepartment of Civil, Structural and Environmental Engineering, University at Buffalo, Buffalo, NY, United States

^bSchool of Engineering and Applied Science, Harvard University, Cambridge, MA, United States

^cKavli Institute for Bionano Science and Technology, Harvard University, Cambridge, MA, United States

ARTICLE INFO

Article history:

Received 11 June 2014

Received in revised form 6 December 2014

Available online 31 December 2014

Keywords:

Phononic crystal

Pattern transformation

Instability

Finite element analysis

ABSTRACT

We investigate the propagation of elastic waves in four periodic porous elastomeric planar structures, where pattern transformation is induced by mechanical instability under uniaxial compression. A series of numerical analyses is performed to offer a detailed understanding of the evolution of their spectral band-gaps as a function of void patterns, porosity, and applied deformation. The results of our study outline a general strategy to design phononic crystals whose response can be effectively tuned by the level of applied deformation.

© 2014 Elsevier Ltd. All rights reserved.

1. Introduction

Phononic crystals are periodic structures designed to control the dispersion of waves through Bragg scattering – the scattering of waves by a periodic arrangement of scatterers with dimensions and periods comparable to the characteristic wavelengths. In the last decade, there has been a growing interest in the study of phononic crystals since they can be engineered to prevent the propagation of elastic waves within a certain range of frequencies called band-gaps (Kushwaha et al., 1993; Jensen, 2003; Martinsson and Movchan, 2003). Because of their band-gap properties, phononic crystals have been exploited to design devices for noise reduction (Casadei et al., 2012), vibration control (Casadei et al., 2010) and wave guides (Vasseur et al., 2007). These practical applications have generated rising interest in the effect of both geometry (Movchan et al., 2006; Bertoldi and Boyce, 2008) and material composition (Vasseur et al., 1994; Cheng et al., 2006; Zhou et al., 2009; Wang et al., 2013) on the location of the band-gaps.

The ability to tune the phononic properties during operation has also been shown to be a promising mechanism to facilitate the engineering applications of phononic crystals (Bertoldi and Boyce, 2008; Wang et al., 2013). It has been demonstrated that both the position and the width of phononic band-gaps can be affected by applied temperature (Jim et al., 2009) and deformation (Bertoldi and Boyce, 2008; Wang and Bertoldi, 2012). Moreover, a

recent study has shown that the tunability of the band-gaps can be significantly increased by enhancing geometric nonlinearity during deformation (Wang et al., 2013). Since geometric nonlinearity can be amplified by triggering instabilities along the loading path, these findings once more highlight the fact that buckling is not always inconvenient or dangerous, but can also be exploited as a new exciting functional actuation mechanism (Bertoldi et al., 2008; Shim et al., 2012, 2013; Babaee et al., 2013).

In a recent study – by considering geometric constraints on the tessellations of the 2D Euclidean plane – it has been shown that in four mono-disperse circular hole arrangements buckling can be exploited to reversibly switch between expanded and folded periodic configurations (Shim et al., 2013). Remarkably, in these structures all the ligaments undergo the first buckling mode in an approximately uniform manner, resulting in a uniform hole closure under deformation and in a homogeneous pattern transformation (see Fig. 1). In this study, we focus on the four planar porous structures shown in Fig. 1 and investigate numerically through finite element simulations the effect of applied deformation on the propagation of elastic waves. In particular, we study how the band-gaps of these structures evolve as a function of void patterns, porosity, and applied deformation, providing guidelines for the design of phononic crystals with desired tunable properties.

2. Formulation

In this section, we present the governing equations and boundary conditions used in the static and wave propagation analyses.

* Corresponding author at: School of Engineering and Applied Science, Harvard University, Cambridge, MA, United States.

2.1. Governing equations

For a given continuum body \mathcal{B} , we denote by Ω_0 and Ω its undeformed (reference) and deformed (current) configurations and by \mathbf{X} and \mathbf{x} material and spatial points in Ω_0 and Ω , respectively. A motion of \mathcal{B} is then a smooth one-to-one mapping that assigns each material point \mathbf{X} to a spacial point \mathbf{x} at time t :

$$\mathbf{x} = \chi(\mathbf{X}, t), \quad x_i = \chi_i(X_i, t). \quad (1)$$

The deformation gradient of the motion is defined as:

$$\mathbf{F} = \text{Grad} \mathbf{x} = \frac{\partial \mathbf{x}}{\partial \mathbf{X}}, \quad F_{ij} = \frac{\partial x_i}{\partial X_j}, \quad (2)$$

where Grad denotes the gradient operator in the undeformed configuration.

In the absence of body forces, the local form of linear momentum balance can be expressed in the undeformed configuration as (Holzapfel, 2000):

$$\text{Div} \mathbf{P} - \rho_0 \frac{D^2 \mathbf{U}}{Dt^2} = \mathbf{0}, \quad \frac{\partial P_{ij}}{\partial X_j} - \rho_0 \frac{D^2 U_i}{Dt^2} = 0, \quad (3)$$

where Div denotes the divergence operator in the undeformed configuration, \mathbf{P} is the first Piola–Kirchhoff stress, $\mathbf{U} = \mathbf{x} - \mathbf{X}$ is the displacement field in the material description, ρ_0 is the mass density in the undeformed configuration and D/Dt denotes the materials time-derivative. For an hyperelastic material with strain energy density function W_0 defined in the undeformed configuration, the first Piola–Kirchhoff stress \mathbf{P} can be expressed as:

$$\mathbf{P} = \frac{\partial W_0}{\partial \mathbf{F}}, \quad P_{ij} = \frac{\partial W_0}{\partial F_{ij}}. \quad (4)$$

Note that the Cauchy stress $\boldsymbol{\sigma}$ is related to the first Piola–Kirchhoff stress by $\boldsymbol{\sigma} = J^{-1} \mathbf{P} \mathbf{F}^T$, where $J = \det \mathbf{F}$.

In order to investigate instabilities and propagation of elastic waves, we consider a perturbation superimposed upon a given state of finite deformation that takes the body to a new equilibrium configuration where (3) is still satisfied. This incremental problem is governed by:

$$\text{Div} \dot{\mathbf{P}} - \rho_0 \frac{D^2 \dot{\mathbf{U}}}{Dt^2} = \mathbf{0}, \quad \frac{\partial \dot{P}_{ij}}{\partial X_j} - \rho_0 \frac{D^2 \dot{U}_i}{Dt^2} = 0, \quad (5)$$

where the accent $\dot{}$ denotes the increment of the corresponding quantity. Moreover, linearization of the constitutive relation yields:

$$\dot{\mathbf{P}} = \mathbb{L} : \dot{\mathbf{F}}, \quad \dot{P}_{ij} = \mathbb{L}_{ijkl} \dot{F}_{kl}, \quad (6)$$

where \mathbb{L} represents the mixed elasticity tensor:

$$\mathbb{L}_{ijkl} = \frac{\partial^2 W_0}{\partial F_{ij} \partial F_{kl}}. \quad (7)$$

The incremental problem can be also described within the deformed configuration. The linearized form of the governing equation can be expressed spatially as:

$$\text{div} \dot{\boldsymbol{\sigma}} - \rho \frac{\partial^2 \dot{\mathbf{u}}}{\partial t^2} = \mathbf{0}, \quad \frac{\partial \dot{\sigma}_{ij}}{\partial x_j} - \rho \frac{\partial^2 \dot{u}_i}{\partial t^2} = 0, \quad (8)$$

where div is the divergence operator with respect to \mathbf{x} and $\partial/\partial t$ is the spatial time derivative and \mathbf{u} represents the displacement field in the spatial description. Employing push-forward transformations based on linear momentum (Wang et al., 2013; Bertoldi and Gei, 2011), we obtain:

$$\dot{\boldsymbol{\sigma}} = J^{-1} \dot{\mathbf{P}} \mathbf{F}^T = \mathbb{C} : \text{grad} \dot{\mathbf{u}}, \quad \dot{\sigma}_{ij} = J^{-1} \dot{P}_{ij} F_{jl} = \mathbb{C}_{ijkl} \frac{\partial \dot{u}_k}{\partial x_l}, \quad (9)$$

where grad denotes the gradient operator in the deformed configuration, and \mathbb{C} represents the spatial elasticity tensor:

$$\mathbb{C}_{ijkl} = J^{-1} F_{jj} F_{ll} \frac{\partial^2 W_0}{\partial F_{ij} \partial F_{kl}}. \quad (10)$$

In this study, we focus on the propagation of infinitesimal amplitude waves described by

$$\dot{\mathbf{u}}(\mathbf{x}, t) = \hat{\mathbf{u}}(\mathbf{x}) e^{-i\omega t}, \quad (11)$$

where $\hat{\mathbf{u}}$ and ω denote the magnitude and angular frequency of the wave, respectively. From the linearized constitutive Eq. (9), $\dot{\boldsymbol{\sigma}}$ is then obtained as:

$$\dot{\boldsymbol{\sigma}}(\mathbf{x}, t) = \hat{\boldsymbol{\sigma}}(\mathbf{x}) e^{-i\omega t}, \quad (12)$$

so that (8) becomes:

$$\text{div} \hat{\boldsymbol{\sigma}} + \rho \omega^2 \hat{\mathbf{u}} = \mathbf{0}, \quad (13)$$

which represents the frequency domain wave equation.

2.2. Elastic waves in 2-D periodic structures

To investigate the propagation of elastic waves in a 2-D infinite periodic structure, we start by defining a primitive unit cell spanned by the lattice primitive vectors \mathbf{a}_1 and \mathbf{a}_2 in its deformed configuration (see Fig. 2(A) and (B)). While any spatially periodic function $v(\mathbf{x})$ is characterized by:

$$v(\mathbf{x} + \mathbf{r}) = v(\mathbf{x}), \quad (14)$$

with

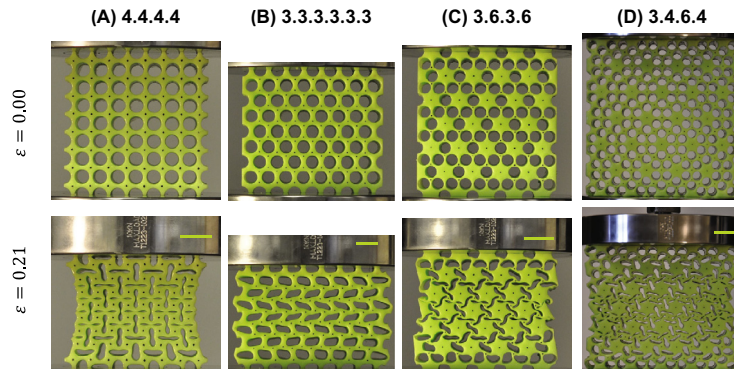


Fig. 1. Experimental images of four periodic structures with differently arranged holes loaded under uniaxial compression in the undeformed (top) and deformed (bottom) configuration (applied compressive engineering strain $\varepsilon = 0.21$) (Shim et al., 2013). All structures are characterized by 50% initial porosity (scale bars: 20 mm). The thin ligaments between the holes are found to buckle in a uniform manner, leading to a distinctive buckled pattern comprising a periodic array of elongated, almost closed ellipses. Since the specimens are made of an elastomeric material, the process is fully reversible and repeatable.

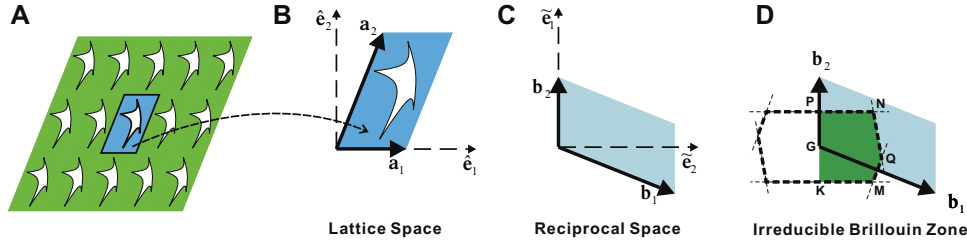


Fig. 2. (A) Schematic of an infinite periodic structure in the two dimensional space. (B) Primitive unit spanned by the primitive lattice vectors \mathbf{a}_1 and \mathbf{a}_2 . Basis vectors are denoted by $\hat{\mathbf{e}}_1$ and $\hat{\mathbf{e}}_2$. (C) The corresponding reciprocal lattice spanned by the reciprocal primitive vectors \mathbf{b}_1 and \mathbf{b}_2 . Basis vectors $\hat{\mathbf{e}}_i$ are defined as $\hat{\mathbf{e}}_i = \frac{2\pi}{\|\mathbf{a}_1 \times \mathbf{a}_2\|} \mathbf{e}_i$ for $i = 1, 2$. (D) The first Brillouin zone corresponds to the polygon enclosed by the dotted lines, and the irreducible Brillouin zone is the green area (enclosed by G-K-M-Q-N-P-G).

$$\mathbf{r} = r_{a1}\mathbf{a}_1 + r_{a2}\mathbf{a}_2, \quad (15)$$

r_{a1} and r_{a2} being arbitrary integers, the propagation of an elastic plane wave within the periodic structure must satisfy the Bloch-periodic conditions (Kittel, 2005):

$$\hat{\Delta}\mathbf{u}(\mathbf{x} + \mathbf{r}) = \hat{\Delta}\mathbf{u}(\mathbf{x})e^{i\mathbf{k}\cdot\mathbf{r}}, \quad (16)$$

where \mathbf{k} denotes the wave vector in the reciprocal space.

Noting that an arbitrary plane wave propagating with a wave vector \mathbf{k} does not necessarily have the periodicity of the structure (i.e., $e^{i\mathbf{k}\cdot\mathbf{r}} \neq 1$ for most \mathbf{k}), we then introduce the reciprocal translational periodicity vectors \mathbf{g} in the wave vector \mathbf{k} -space:

$$\mathbf{g} = g_{b1}\mathbf{b}_1 + g_{b2}\mathbf{b}_2, \quad (17)$$

where g_{b1} and g_{b2} are arbitrary integers and the reciprocal primitive lattice vectors \mathbf{b}_1 and \mathbf{b}_2 are defined as:

$$\mathbf{b}_1 = 2\pi \frac{\mathbf{a}_2 \times \hat{\mathbf{e}}_3}{\|\mathbf{a}_1 \times \mathbf{a}_2\|}, \quad \mathbf{b}_2 = 2\pi \frac{\hat{\mathbf{e}}_3 \times \mathbf{a}_1}{\|\mathbf{a}_1 \times \mathbf{a}_2\|}, \quad (18)$$

with $\hat{\mathbf{e}}_3 = (\mathbf{a}_1 \times \mathbf{a}_2) / \|\mathbf{a}_1 \times \mathbf{a}_2\|$ (see Fig. 2(C)). Since $\mathbf{a}_i \cdot \mathbf{b}_j = 2\pi\delta_{ij}$ (δ_{ij} here is the Kronecker delta), it is easy to show that $e^{i\mathbf{g}\cdot\mathbf{r}} = 1$, yielding

$$e^{i\mathbf{g}\cdot(\mathbf{x}+\mathbf{r})} = e^{i\mathbf{g}\cdot\mathbf{x}}. \quad (19)$$

Combining (16) and (19), we can see that the wave motion is \mathbf{g} -periodic in the reciprocal wave vector \mathbf{k} -space (i.e. $\hat{\Delta}\mathbf{u}_{\mathbf{k}+\mathbf{g}}(\mathbf{x} + \mathbf{r}) = \hat{\Delta}\mathbf{u}_{\mathbf{k}}(\mathbf{x} + \mathbf{r})$), so that the eigenvalues $\omega(\mathbf{k})$ of the frequency domain wave Eq. (13) are also \mathbf{g} -periodic in \mathbf{k} (Kittel, 2005),

$$\omega(\mathbf{k} + \mathbf{g}) = \omega(\mathbf{k}). \quad (20)$$

Thus, only a subset of wave vectors \mathbf{k} is needed to be considered to calculate the dispersion relation. Such subset spans the first Brillouin zone (Brillouin, 1946), which corresponds to the polygonal area enclosed by the perpendicular bisectors of the reciprocal lattice vectors (see dotted polygon in Fig. 2(D)). Moreover, if the primitive unit cell is invariant under certain rotational or mirror reflectional transformations, only part of the first Brillouin zone needs to be considered, which is referred as the irreducible Brillouin zone (IBZ) (see the shaded region within the hexagon in Fig. 2(D)). Finally, to construct the dispersion relation for periodic structures with symmetries it is a common practice to consider only wave vectors on the boundary of the irreducible Brillouin zone (Maldovan and Thomas, 2009).

3. Numerical strategies

In this study, both the static and dynamic response of infinite periodic 2-D structures is investigated using the commercial finite element software ABAQUS/Standard and considering a unit cell with suitable boundary conditions.

3.1. Static analysis

To determine the static response of an infinite structure subjected to a macroscopic deformation gradient $\bar{\mathbf{F}}$, periodic boundary conditions are imposed to the boundary of a spatially periodic unit cell such that

$$\mathbf{u}_\beta = \mathbf{u}_\alpha + (\bar{\mathbf{F}} - \mathbf{1})(\mathbf{X}_\beta - \mathbf{X}_\alpha), \quad (21)$$

where the subscripts α and β are two nodal points periodically located on the boundary of the unit cell and $\mathbf{1}$ denotes the second order identity tensor. Within the finite element framework, the components of $\bar{\mathbf{F}}$ can be conveniently prescribed using a set of virtual nodes and the corresponding macroscopic first Piola–Kirchhoff stress $\bar{\mathbf{P}}$ is then obtained through virtual work consideration (Danielsson et al., 2002; Bertoldi and Boyce, 2008). Note that, if a microscopic instability is detected along the loading path, an enlarged primitive unit is used with the size dictated by the new periodicity of the buckled structure. Moreover, to trigger the instability during the simulation and to capture the post-transformation behavior, a small imperfection¹ based on first three eigenmodes of the enlarged primitive unit is introduced into the mesh by perturbing the initial position of each node.

3.2. Stability analysis

Upon application of deformation, an infinitely periodic structure can suddenly change its periodicity due to mechanical instability. Such instability could be either microscopic (i.e., with wavelengths that are of the order of the size of the microstructure) or macroscopic (i.e., with much larger wavelengths than the size of the microstructure) (Triantafyllidis and Maker, 1985; Geymonat et al., 1993; Bertoldi and Boyce, 2008).

3.2.1. Microscopic instability

Microscopic (local) buckling modes are characterized by wavelengths that are of the order of the size of the microstructure and may alter the initial periodicity of the solid. The simplest, but computationally expensive path for investigating them is to construct enlarged unit cells of various sizes spanned by lattice vectors $\hat{\mathbf{a}}_1 = m_1\mathbf{a}_1$ and $\hat{\mathbf{a}}_2 = m_2\mathbf{a}_2$ (m_1 and m_2 being positive integers)² and to use a linear perturbation procedure to calculate their critical strains and corresponding modes. The critical strain of the infinite periodic structure is then defined as the minimum of the critical strains on all possible enlarged unit cells (Bertoldi et al., 2008; Kang et al., 2014).

Interestingly, the computational cost of such analysis can be significantly reduced considering a single primitive unit cell and

¹ The imperfection amplitude for each mode was chosen to be smaller than 1 % of the average element size in the finite element model.

² Note that the accent ^ is used here to identify quantities related to the enlarged unit cell.

applying Bloch-periodic conditions (16) (Triantafyllidis and Maker, 1985; Geymonat et al., 1993; Bertoldi and Boyce, 2008) with

$$\hat{\mathbf{k}} = \hat{\mathbf{b}}_1 + \hat{\mathbf{b}}_2, \quad (22)$$

where

$$\hat{\mathbf{b}}_1 = \frac{1}{m_1} \mathbf{b}_1, \quad \text{and} \quad \hat{\mathbf{b}}_2 = \frac{1}{m_2} \mathbf{b}_2. \quad (23)$$

In fact, it follows from (16) that for any choice of m_1 and m_2

$$\hat{\Delta} \mathbf{u}(\mathbf{x} + \hat{\mathbf{a}}_1 + \hat{\mathbf{a}}_2) = \hat{\Delta} \mathbf{u}(\mathbf{x}) e^{i\hat{\mathbf{k}} \cdot (\hat{\mathbf{a}}_1 + \hat{\mathbf{a}}_2)} = \hat{\Delta} \mathbf{u}(\mathbf{x}), \quad (24)$$

clearly indicating that $\hat{\mathbf{k}}$ can be used on a single primitive unit cell for the analysis of the response of the enlarged unit cell spanned by $\hat{\mathbf{a}}_1$ and $\hat{\mathbf{a}}_2$. To work with the complex-valued relations of the Bloch-periodic conditions (16) in ABAQUS, all fields are split into real and imaginary parts. In this way, the equilibrium equations are divided into two sets of uncoupled equations for the real and imaginary parts (Aberg and Gudmundson, 1997; Bertoldi and Boyce, 2008). Thus, the problem is solved using two identical finite-element meshes for the unit cell, one for the real part and the other for the imaginary part, and coupling them by Bloch-periodic displacement boundary conditions:

$$\begin{aligned} \hat{\Delta} \mathbf{u}_{\beta}^{\text{re}} &= \hat{\Delta} \mathbf{u}_{\alpha}^{\text{re}} \cos[\mathbf{k} \cdot \mathbf{r}_{\alpha\beta}] - \hat{\Delta} \mathbf{u}_{\alpha}^{\text{im}} \sin[\mathbf{k} \cdot \mathbf{r}_{\alpha\beta}], \\ \hat{\Delta} \mathbf{u}_{\beta}^{\text{im}} &= \hat{\Delta} \mathbf{u}_{\alpha}^{\text{re}} \sin[\mathbf{k} \cdot \mathbf{r}_{\alpha\beta}] + \hat{\Delta} \mathbf{u}_{\alpha}^{\text{im}} \cos[\mathbf{k} \cdot \mathbf{r}_{\alpha\beta}], \end{aligned} \quad (25)$$

where $\mathbf{r}_{\alpha\beta} = \mathbf{x}_{\beta} - \mathbf{x}_{\alpha}$ denotes the distance in the deformed configuration between two nodes periodically located on the primitive unit boundary, and the superscripts re and im denote the real and the imaginary part of the displacement field, respectively. Note that (25) can be easily implemented within ABAQUS/Standard using a user defined subroutine MPC (ABAQUS, 2010).

The stability of each enlarged unit defined by m_1 and m_2 can be then investigated within the finite element framework by detecting the point along the loading path at which the corresponding tangent stiffness matrix becomes singular (i.e., $\det[K] = [0]$). Alternatively, the stability of each enlarged unit cell can be investigated by detecting the applied load at which the smallest eigenfrequency associated to a non-trivial eigenmode is zero (Bathe, 1996). Finally, the onset of instability for the infinite periodic structure is defined as the minimum critical strain on all the considered enlarged unit cells defined by m_1 and m_2 . Here, we investigated the stability of 25 enlarged primitive units by choosing $m_1 = 1, \dots, 5$ and $m_2 = 1, \dots, 5$ in (23). To detect the onset of instability for each enlarged primitive unit, we perform eigenfrequency analysis (module *FREQUENCY in ABAQUS) along the loading path at increasing values of applied deformation and detect the smallest load for which an eigenfrequency associated with a non-trivial eigenmode becomes zero.³ The critical strain of the infinite periodic structure is then defined as the minimum on all 25 considered enlarged unit cells.

3.2.2. Macroscopic instability

It has been shown that macroscopic, long wavelength instabilities correspond to loss of ellipticity at the macroscopic scale (Geymonat et al., 1993). Therefore, they can be investigated by detecting when the homogenized mixed elasticity tensor $\bar{\mathbb{L}}$ violates the positive definite conditions (Marsden and Hughes, 1983):

$$(\mathbf{m} \otimes \mathbf{N}) : \bar{\mathbb{L}} : (\mathbf{m} \otimes \mathbf{N}) > 0, \quad \bar{\mathbb{L}}_{ijkl} m_i N_j m_k N_l > 0 \quad (26)$$

for all $\mathbf{m} \otimes \mathbf{N} \neq \mathbf{0}$, where \mathbf{m} and \mathbf{N} are unit vectors defined in the deformed and the undeformed configurations, respectively. Note that the homogenized mixed elasticity tensor $\bar{\mathbb{L}}$ relates the macroscopic deformation gradient increment $\bar{\mathbf{F}}$ to the macroscopic first Piola–Kirchhoff stress increment $\bar{\mathbf{P}}$ as:

$$\bar{\mathbf{P}} = \bar{\mathbb{L}} : \bar{\mathbf{F}}, \quad \bar{\mathbf{P}}_{ij} = \bar{\mathbb{L}}_{ijkl} \bar{\mathbf{F}}_{kl}. \quad (27)$$

In this study, 2-D finite element simulations on a single primitive unit cell with the spatially periodic boundary conditions (14) are performed to monitor the loss of ellipticity of the homogenized tangent modulus $\bar{\mathbb{L}}$. At every deformation increment, the components of $\bar{\mathbb{L}}$ are identified by subjecting the unit cells to four independent linear perturbations of the macroscopic deformation gradient $\bar{\mathbf{F}}$, calculating the corresponding averaged stress components $\bar{\mathbf{P}}$ and comparing to Eq. (27). Then, the loss of ellipticity condition is examined by checking the positive definite condition (26) with \mathbf{m} and \mathbf{N} separately explored at every $\pi/360$ radian increment.

3.3. Wave propagation analysis

To calculate the dispersion relation $\omega = \omega(\mathbf{k})$ within the finite element framework, the Bloch-periodic conditions (16) are applied to the boundary of the enlarged unit cell as described in Section 3.2.1. As mentioned in Section 2, only wavevectors located on the perimeter of the IBZ are considered (i.e., the edges of the green area in Fig. 2(D)). In particular, we discretize each edge of the IBZ into 20 segments of equal length, so that

$$\mathbf{k}_{j,G-K} = \mathbf{k}_G + \frac{j}{N} [\mathbf{k}_G - \mathbf{k}_K] \quad \text{for } j = 0, 1, 2, \dots, N \quad \text{with } N = 20, \quad (28)$$

where $\mathbf{k}_{j,G-K}$ denotes the j th wave vector between two adjacent vertices G and K in the wave vector \mathbf{k} -space. For each considered wave vector \mathbf{k} , the corresponding frequencies ω are then calculated performing an eigenfrequency analysis. The eigenfrequencies associated with each considered wavevector are then plotted in the dispersion relation diagram, where phononic band-gaps can be readily identified.

Since the goal of our study is to evaluate the effect of applied deformation to the propagation of elastic waves in periodic structures undergoing microscopic instabilities, we first perform a static analysis on the enlarged unit cell (with dimensions dictated by the microscopic instability analysis) subject to the prescribed deformation $\bar{\mathbf{F}}$. The static analysis is then followed by eigenfrequency wave analyses, which account for the effect of the pre-deformation. It is important to note that applied deformation leads to a change of the primitive lattice vectors:

$$\mathbf{a}_1 = \bar{\mathbf{F}} \mathbf{A}_1, \quad \mathbf{a}_2 = \bar{\mathbf{F}} \mathbf{A}_2, \quad (29)$$

where \mathbf{A}_i and \mathbf{a}_i ($i = 1, 2$) denote the vectors in the undeformed and the deformed configurations, respectively. Therefore, the Brillouin zone also evolves during deformation, and we account for this in the calculations.

4. Numerical results

In this section, after describing the geometry, material model and loading conditions, we present numerical results for the static and dynamic response of periodic 2-D porous structures, characterized by instability-induced pattern transformation under uniaxial compression. Our results demonstrate that the band-gaps of the considered structures are highly affected not only by hole arrangement and porosity, but also by applied deformation. Note that all

³ Note that this procedure is significantly simpler than calculating $\det[K] = [0]$, since it does not require to export the stiffness matrix calculated by ABAQUS and to evaluate its determinant using a numerical package.

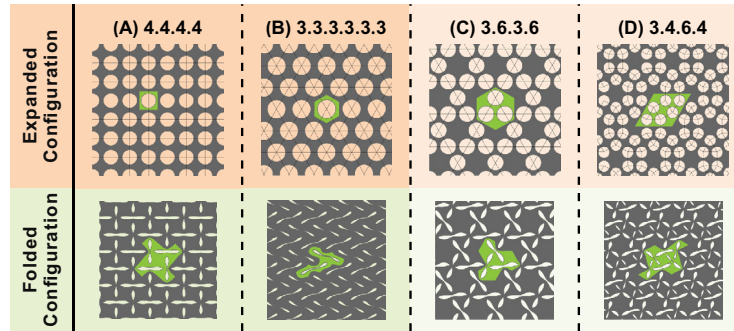


Fig. 3. Four mono-disperse circular hole arrangements where buckling can be exploited to reversibly switch between expanded and folded periodic configurations: (A) square, (B) triangular, (C) rhombille and (D) deltoidal trihexagonal arrangements of holes. The expanded periodic configurations are constructed starting from uniform tilings, which can be completely described by their vertex figure (*i.e.*, a sequence of numbers representing the number of edges of the polygons going around the vertex) indicated at the top of each column.

simulations were performed using the nonlinear finite-element package ABAQUS/Standard.

4.1. Geometry, materials and loading conditions

Geometry. We investigate the response of four periodic porous structures for which buckling can be exploited to reversibly switch between expanded and folded periodic configurations (Shim et al., 2013). In Fig. 3 we show the hole arrangements considered in this study, corresponding to a square (*i.e.* here and in the following identified by its vertex configuration⁴ 4.4.4.4), hexagonal (3.3.3.3.3.3), rhombille (3.6.3.6) and deltoidal trihexagonal (3.4.6.4) tilings in both the undeformed (expanded) and deformed (folded) configurations.

In all these structures, the minimum width of the ligaments between adjacent holes is given by $(A_0 - 2R_0)$, A_0 and R_0 denoting the center-to-center distance between holes and the hole radius in the undeformed configuration (see Fig. 5), respectively. Since the phononic band-gaps are strongly influenced by the smallest geometric feature in the system (Liu et al., 2002), here we compare the response of structures characterized by the same ratio R_0/A_0 . Note that the same ratio of R_0/A_0 leads to different values of initial porosity ψ_0 in the four periodic patterns under investigation. For example, $R_0/A_0 = 0.47$ results in an initial porosity $\psi_0 = 0.69, 0.80, 0.60$ and 0.64 for structures 4.4.4.4, 3.3.3.3.3.3, 3.6.3.6 and 3.4.6.4, respectively.

In all our analyses, plane strain conditions are assumed and 2-D models are constructed using 6-node modified hybrid elements (elements CPE6MH in ABAQUS). The accuracy of the meshes was ascertained through a mesh refinement study, resulting in the final sweeping seed size of $0.07A_0$ to ensure mesh convergence in all simulations. Note that for a given a set of geometric parameters, the same finite element model was used for both the static as well as the wave propagation analysis.

Constituent material properties. The response of the material is captured using the Yeoh hyperelastic model (Yeoh, 1993) whose strain energy density is given by

$$W_0 \equiv \sum_{i=1}^3 \left[C_{i0} (\bar{I}_1 - 3)^i + (J - 1)^{2i} / D_i \right], \quad (30)$$

where $J = \det(\mathbf{F})$ and $\bar{I}_1 = \text{tr}(J^{-2/3} \mathbf{F}^T \mathbf{F})$. Note that two of the parameters entering in the Yeoh model are related to the conventional shear modulus (G_0) and bulk modulus (K_0) at zero strain as $C_{10} = G_0/2$ and $D_1 = 2/K_0$. Here, we use $C_{10} = 131$ kPa, $C_{20} = 0$ kPa, $C_{30} = 3.5$ kPa, and $D_1 = D_2 = D_3 = 38.2$ GPa⁻¹ and an initial

⁴ For uniform tiling, the vertex configuration is a sequence of numbers representing the number of sides of the faces going around the vertex.

mass density of $\rho_0 = 965$ kg/m³, which are suitable for describing a silicone rubber (Vinylpolysiloxane: Elite Double 32, Zhermack) (Shim et al., 2012).

Loading conditions. In this study, assuming plane strain conditions, we consider infinitely periodic structures under uniaxial compression, so that

$$\bar{\mathbf{F}} = (1 + \varepsilon_{11}) \hat{\mathbf{e}}_1 \otimes \hat{\mathbf{e}}_1 + (1 - \varepsilon) \hat{\mathbf{e}}_2 \otimes \hat{\mathbf{e}}_2 + \hat{\mathbf{e}}_3 \otimes \hat{\mathbf{e}}_3, \quad (31)$$

where ε denotes the applied compressive engineering strain in x_2 -direction, and ε_{11} is determined from $\sigma_{11} = 0$. Here, a compressive engineering strain of $\varepsilon = 0.2$ is applied to investigate the effect of the non-linear deformation on the propagation of small amplitude elastic waves.

4.2. Stability analysis

Finite element simulations are performed on the four unit cells highlighted in Fig. 3-top to detect both macroscopic and microscopic instabilities under uniaxial compression. Structures characterized by a wide range of aspect ratios, $R_0/A_0 \in (0.37, 0.48)$, are considered and the results are summarized in Fig. 4, where the critical engineering strains at the onset of both microscopic and macroscopic instabilities are reported as a function of both R_0/A_0 (bottom horizontal axis) and the initial porosity ψ_0 (top horizontal axis). Regardless of the type of instability and hole arrangement, the critical strain is found to monotonically decrease for increasing values of R_0/A_0 due to the reduction of structural stiffness. Moreover, within the considered range of initial porosity, the critical strain for microscopic instability is found to be always smaller than that corresponding to macroscopic instability, so that short wavelength modes are expected to emerge along the loading path for all the four porous structures. Note that the microscopic instability alters the initial periodicity of structures 4.4.4.4 and 3.3.3.3.3.3, so that enlarged primitive cells consisting of 2×2 and 1×2 of initial primitive units are required to describe the post-buckling response of these structures, respectively. In contrast, structures 3.6.3.6 and 3.4.6.4 are found to retain their initial periodicity even after the onset of instability.

4.3. Wave propagation analysis: design of tunable phononic crystals

We now investigate the effects of the hole pattern, the ratio R_0/A_0 and the applied compressive strain on the band-gaps of the four periodic structures shown in Fig. 3-top. In order to study the propagation of waves in these structures, we use unit cells with the size dictated by the periodicity introduced by buckling (see Fig. 5). It is important to note that the alteration in periodicity induced by buckling significantly affects both the shape and the

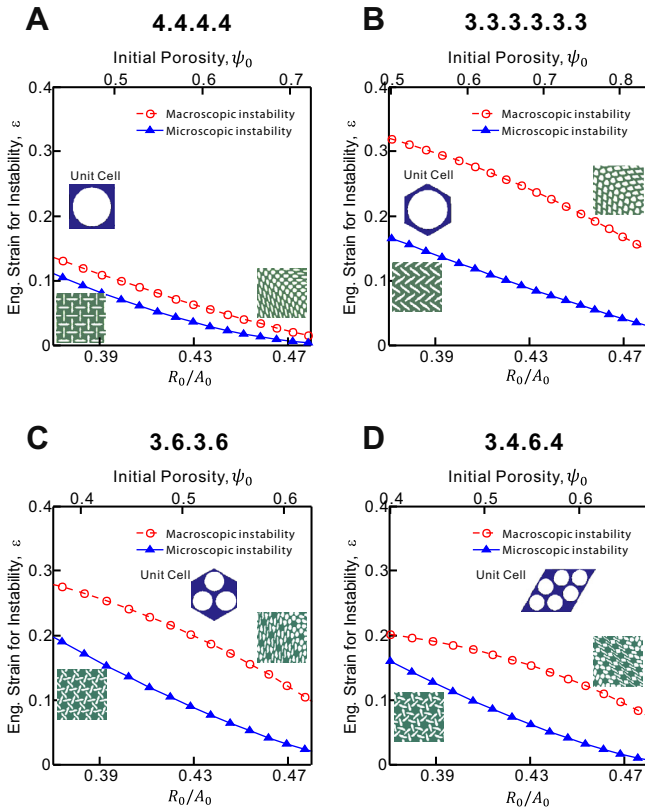


Fig. 4. Simulation results of instability analyses for structures (A) 4.4.4.4, (B) 3.3.3.3.3.3, (C) 3.6.3.6 and (D) 3.4.6.4.

size of the IBZ (e.g., the IBZ for structure 4.4.4.4 shrinks to a quarter of its initial size after buckling.). However, since in our calculations we use the enlarged unit cells predicted by the stability analysis (see Fig. 5), we only need to account for the gradual increase of the IBZ induced by the applied finite deformation.

We start by constructing the dispersion diagrams for the undeformed configurations, which are shown in Fig. 6 in terms of normalized frequency $\tilde{\omega} = \omega A_0 / (2\pi c_T)$, where $c_T = \sqrt{G_0/\rho_0}$ is the transverse plane wave velocity in the homogeneous material. While several studies have focused on the band-gaps in the undeformed configuration of structures 4.4.4.4 and 3.3.3.3.3.3 (Zalipaev et al., 2002; Wu et al., 2004; Bertoldi and Boyce, 2008; Su et al., 2012), little is known about structures 3.6.3.6 and 3.4.6.4. It is interesting to see that these latter structures are characterized by rather low frequency band-gaps occurring near $\tilde{\omega} \sim 0.4$, highlighting once more the important role played by the hole pattern.

Next, to investigate the effect of applied deformation on the propagation of elastic waves, we compress uniaxially all the structures by applying a compressive engineering strain up to $\varepsilon = 0.2$ and then construct the dispersion diagrams for the deformed configurations (see Fig. 7). By comparing the plots reported in Figs. 6

and 7, it is easy to see that the applied deformation substantially alters the band-gaps as well as the IBZ.

To better quantify this effect we now proceed by calculating the band-gaps for all four structures at several points along the loading path. In particular, we consider structure characterized by $R_0/A_0 = 0.43, 0.45$ and 0.47 , apply compressive engineering strains up to $\varepsilon = 0.2$ and calculate the band diagram after every strain increment of $\Delta\varepsilon = 0.005$. These calculations enable us to describe the transformations of the band-gaps as a function of applied deformation, as shown in Fig. 8–11 for structures 4.4.4.4, 3.3.3.3.3.3, 3.6.3.6 and 3.4.3.6, respectively.

4.3.1. 4.4.4.4 and 3.3.3.3.3.3: Band-gap structures with low tunability

We start by discussing the results for structure 4.4.4.4, for which the ratios $R_0/A_0 = 0.43, 0.45$, and 0.47 correspond to an initial porosity $\psi_0 = 0.58, 0.64$, and 0.69 , respectively. The deformed shapes and the corresponding dispersion relations at different levels of compressive engineering strain are provided in Fig. 8. As shown in Fig. 8-top, in the undeformed configuration this structure possesses a phononic band-gap near $\tilde{\omega} \sim 0.7$ for all three values of R_0/A_0 .

As R_0/A_0 increases, this band-gap tends to increase in width and to migrate to lower frequencies because of the reduction of structural stiffness induced by the increase in porosity. The results reported in Fig. 8 also highlight the effect of applied deformation on the propagation of elastic waves in the structure. Up to the onset of the microscopic instability (corresponding to the red vertical line in Fig. 8), no significant changes in the band-gap are observed. However, as the new pattern induced by buckling becomes more accentuated (i.e., $\varepsilon > 0.1$) a couple of new band-gaps open. Moreover, it is worth noticing that applied deformation also alters the IBZ, and thus both undeformed and deformed (at $\varepsilon = 0.2$) IBZs are reported in the inserts of Fig. 8. Since the size of the reciprocal lattice of a periodic 2-D structure is inversely proportional to the area spanned by the primitive lattice vectors, the size of IBZ increases as applied deformation reduces the porosity of the structure.

Fig. 9 shows the results for structure 3.3.3.3.3.3. For the case of small R_0/A_0 (e.g. 0.43 in 9A), this structure hardly possesses any band-gap in both undeformed and deformed configurations. Differently, for larger R_0/A_0 (e.g. 0.45 and 0.47 in 9B and 9C, respectively), the structure is characterized by a band-gap in the undeformed state, but its width is much smaller than that found in the undeformed structure 4.4.4.4. When the structure is deformed, this band-gap gradually fades out and then appears again when the deformation is further increased.

4.3.2. 3.6.3.6 and 3.4.6.4: Band-gap structures with high tunability

Next, we focus on the effect of applied deformation on the propagation of elastic waves in structures 3.6.3.6 and 3.4.6.4. Remarkably, the results reported in Figs. 10 and 11 clearly indicate that these two structures offer higher band gap tunability than structures 4.4.4.4 and 3.3.3.3.3.3.

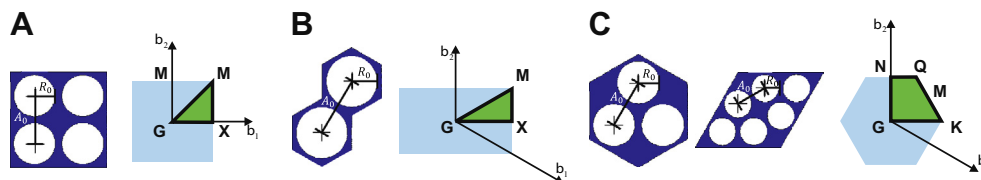


Fig. 5. Representative volume elements as predicted by the stability analysis and the corresponding irreducible Brillouin zones (IBZ) in the reciprocal space: (A) 4.4.4.4, (B) 3.3.3.3.3.3, (C) 3.6.3.6, and 3.4.6.4. Note that, although the unit cells for structures 3.6.3.6, and 3.4.6.4 have different shapes, their corresponding IBZs are identical. In the simulations we account for the gradual increase of the IBZ induced by the applied finite deformation.

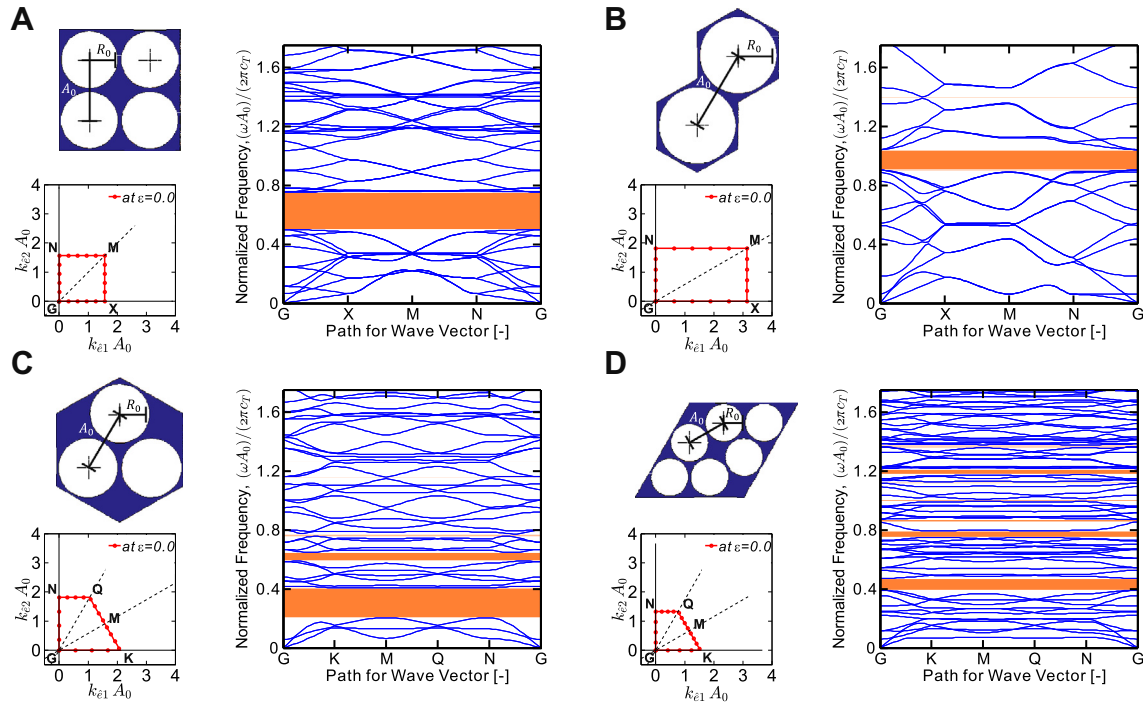


Fig. 6. Dispersion relations for the undeformed structures with $R_0/A_0 = 0.47$. (A) 4.4.4.4, (B) 3.3.3.3.3.3, (C) 3.6.3.6, and (D) 3.4.3.6.

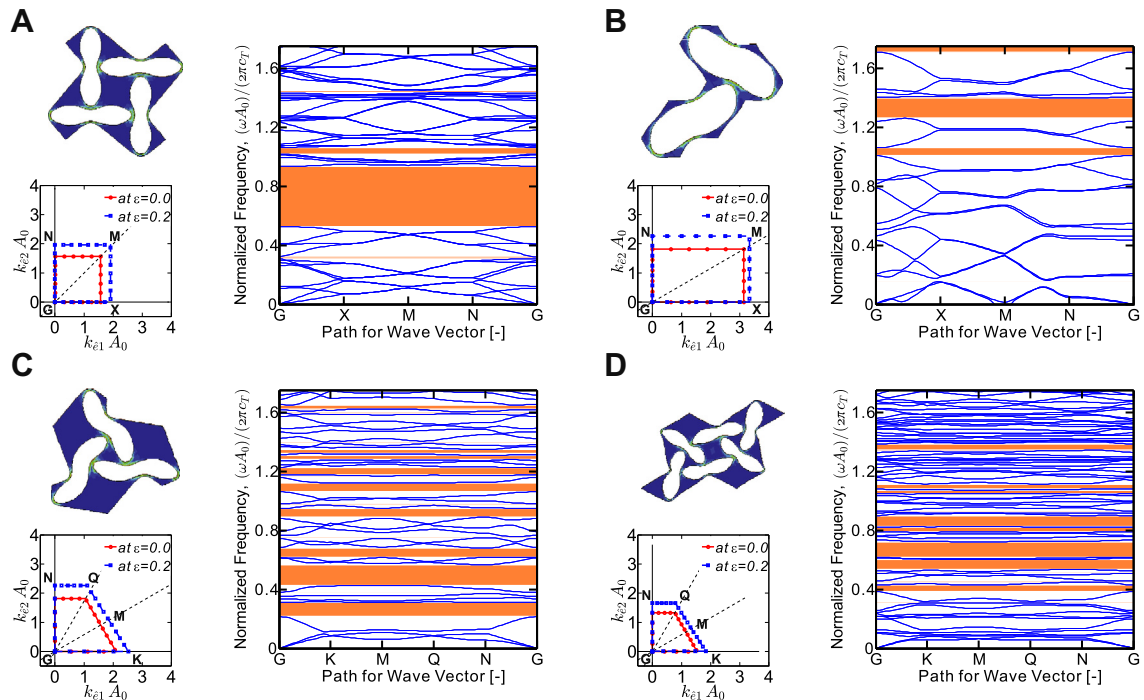


Fig. 7. Dispersion relations for the deformed structures (at the compressive engineering strain of $\varepsilon = 0.2$) with $R_0/A_0 = 0.47$ (A) 4.4.4.4, (B) 3.3.3.3.3.3, (C) 3.6.3.6, and (D) 3.4.3.6.

Focusing on Fig. 10, where we report results for structure 3.6.3.6, we note that the undeformed configuration is characterized by a wide band-gap at $\tilde{\omega} \in (0.28, 0.43)$, $(0.25, 0.44)$, and $(0.20, 0.41)$ for $R_0/A_0 = 0.43, 0.45$, and 0.47 , respectively. Note that these band-gaps are located at much lower frequency ranges than those of structures 4.4.4.4 and 3.3.3.3.3.3, making this hole arrangement a promising candidate for engineering applications. Furthermore, as the applied compressive strain is increased and

the folded pattern induced by instability emerges, several new band-gaps open and this process becomes more accentuated as the ratio R_0/A_0 increases.

Finally, the results reported in Fig. 11 show that structure 3.4.6.4 is characterized by a similar response. Although in the undeformed configuration the system possess only few low frequency band-gaps, these are significantly altered by applied deformation and the effect is enhanced for increasing values of porosity.

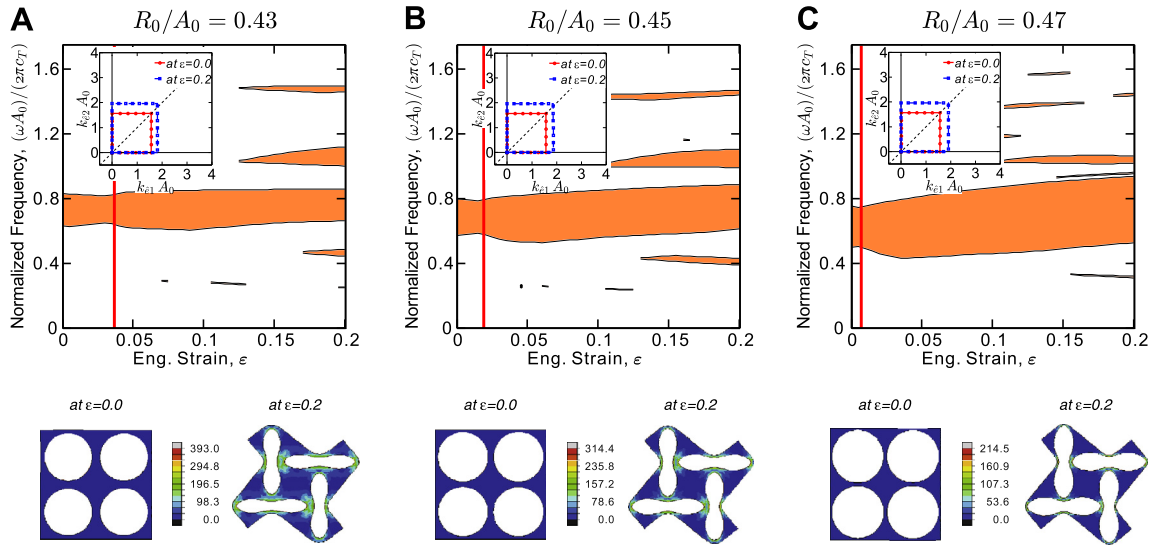


Fig. 8. Phononic band-gaps as a function of the applied strain for structure 4.4.4.3.3.3 subjected to uniaxial compression. Three different aspect ratios are presented: (A) $R_0/A_0 = 0.43$, (B) $R_0/A_0 = 0.45$, and (C) $R_0/A_0 = 0.47$. The contour plot on the deformed structures represents the von-Mises stress distribution (unit: kPa), and the inserted figures shows the change of the IBZ during the corresponding pattern transformation.

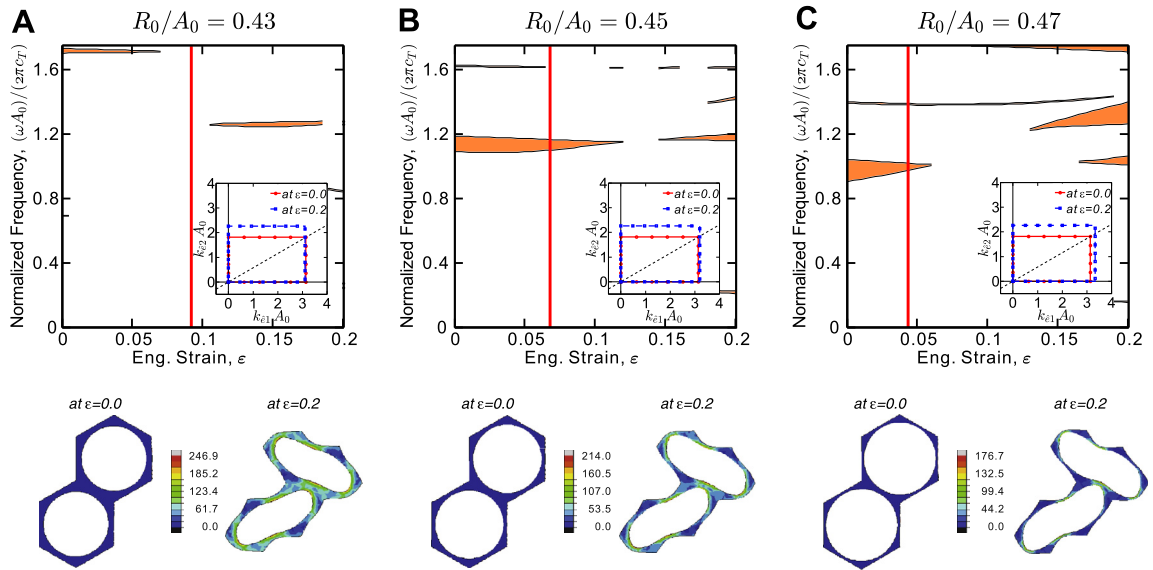


Fig. 9. Phononic band-gaps as a function of the applied strain for structure 3.3.3.3.3.3.3 subjected to uniaxial compression. Three different aspect ratios are presented: (A) $R_0/A_0 = 0.43$, (B) $R_0/A_0 = 0.45$, and (C) $R_0/A_0 = 0.47$. The contour plot on the deformed structures represents the von-Mises stress distribution (unit: kPa), and the inserted figures shows the change of the IBZ during the corresponding pattern transformation.

Therefore, our numerical results indicate that structure 3.6.3.6 and 3.4.6.4 characterized by large values of porosity can be an excellent candidate for the design of tunable systems, since a wide range of frequencies can be switched on/off by applied deformation.

4.3.3. Discussion and conclusions

In this study, we numerically investigate the propagation of small amplitude elastic waves in four porous elastomeric structures, in which a mechanical instability under uniaxial compression induces a pattern transformation. Our study shows that mechanical instabilities and large deformation can be effectively utilized to reversibly tune and control the phononic band gaps of the periodic structures. More specifically, our results indicate that:

(i) For a given value of applied strain ϵ and hole pattern, an increase in porosity results in wider band-gaps.

(ii) For a given value of applied compressive strain ϵ and ratio R_0/A_0 , the hole pattern has a strong effect on the number and location of the band-gaps. While this observation is well known for the undeformed structures (Maldovan and Thomas, 2009), our study show that it also applies to the deformed configurations. In fact, with the exception of structure 3.3.3.3.3.3.3, all other three structures are characterized by several low-frequency band-gaps along the entire deformation process, whose location and width is found to be determined by the hole arrangement, the porosity and the level of applied deformation.

(iii) For a given ratio R_0/A_0 and a given hole pattern, the pattern transformation induced by instability plays a key role in the evolution of the band-gaps. Initially, the structure deforms in an affine manner and the band-gaps are only marginally affected by the applied compressive strain. However, as the folded pattern emerges beyond the onset of instability, the width of the pre-existing band-gaps significantly changes and

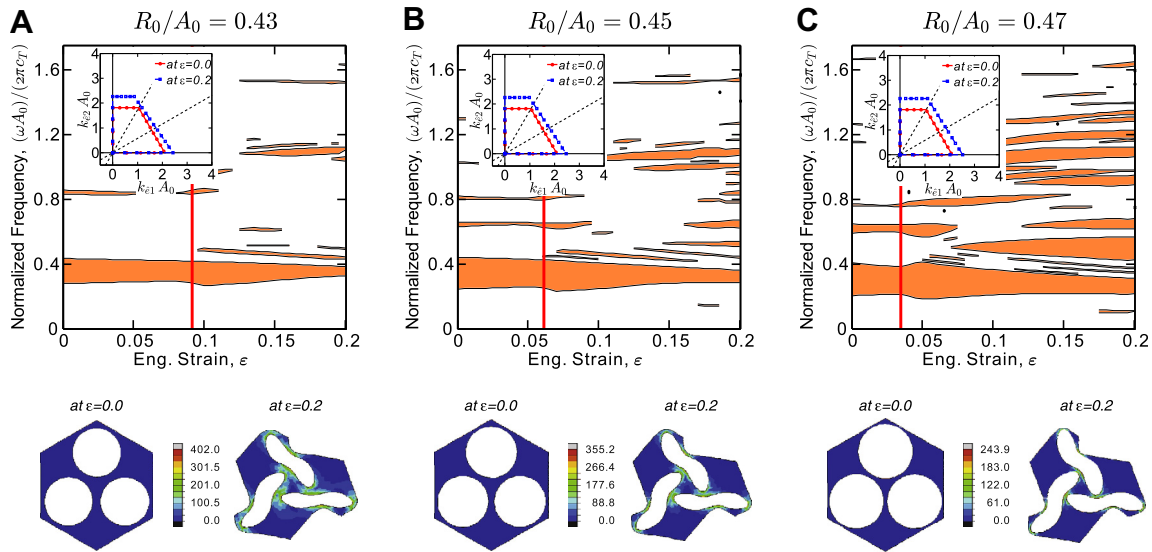


Fig. 10. Phononic band-gaps as a function of the applied strain for structure 3.6.3.6 subjected to uniaxial compression. Three different aspect ratios are presented: (A) $R_0/A_0 = 0.43$, (B) $R_0/A_0 = 0.45$, and (C) $R_0/A_0 = 0.47$. The contour plot on the deformed structures represents the von-Mises stress distribution (unit: kPa), and the inserted figures shows the change of the IBZ during the corresponding pattern transformation.

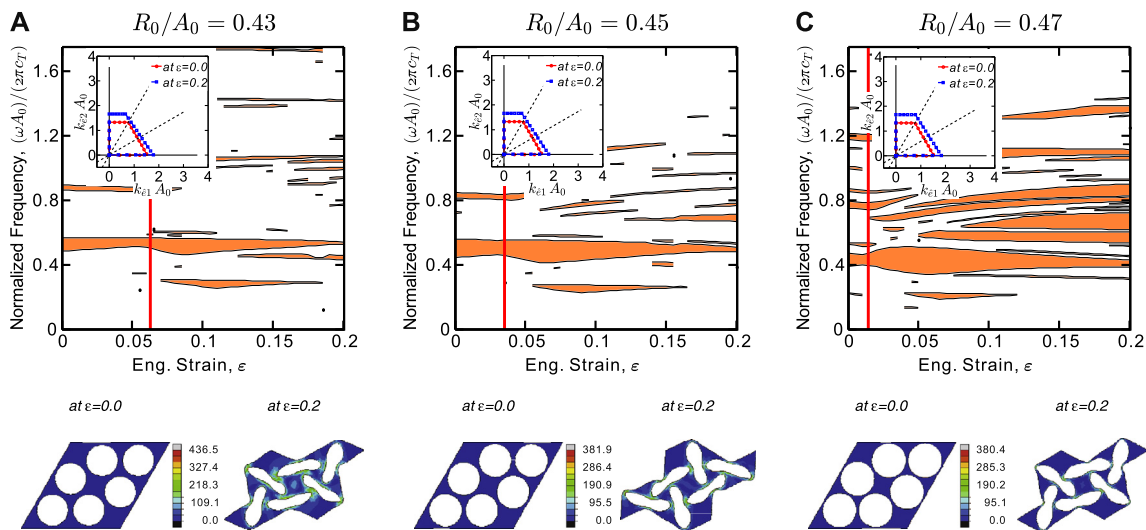


Fig. 11. Phononic band-gaps as a function of the applied strain for structure 3.4.6.4 subjected to uniaxial compression. Three different aspect ratios are presented: (A) $R_0/A_0 = 0.43$, (B) $R_0/A_0 = 0.45$, and (C) $R_0/A_0 = 0.47$. The contour plot on the deformed structures represents the von-Mises stress distribution (unit: kPa), and the inserted figures shows the change of the IBZ during the corresponding pattern transformation.

several new band-gaps open. In particular, structures 3.6.3.6 and 3.4.6.4 with higher R_0/A_0 ratios show dramatic changes in the band-gap distribution induced by the applied deformation. (iv) It is worthwhile to mention that the deformed configurations of structures 3.6.3.6 and 3.4.6.4 are chiral. Although structural chirality is known to have no effect on the mechanical properties of materials based on classical elasticity (Lakes, 2001), this study shows that the considered chiral structures have superior low-frequency band-gap capabilities, as previously shown by Spadoni et al. (2009). However, the investigation of the connections between chirality and propagation of elastic waves goes beyond the scope of the present work and will be the subject of future research.

We also note that in order for the structures to sustain the large deformation induced by buckling while remaining in the fully

elastic regime, elastomeric materials such as silicon rubber are typically used for fabrication. Although these materials are dissipative and it is well known that material damping affects the dynamic response of the system (Psarobas, 2001; Jensen, 2003; Liu et al., 2008; Hussein, 2009), here we consider them to be purely elastic. This choice is motivated by the fact that it has been recently shown that moderate levels of damping as those provided by elastomeric materials do not significantly affect the band-gaps of the periodic structures (Babae et al., submitted for publication).

In conclusion, our study outlines a general strategy in which a judicious choice of hole arrangement and porosity provides a foundation for the design of phononic crystals whose response can be tuned by applied deformation. Furthermore, since buckling is scale independent and the deformation process is fully reversible, we expect our results will contribute the design of smart

systems that control the wave propagation depending on applied deformation.

Acknowledgements

This work has been partially supported by the Harvard Materials Research Science and Engineering Center under NSF award number DMR-1420570 and by NSF through Grants CMMI-1120724 and CMMI-1149456 (CAREER). K.B. acknowledges start-up funds from the Harvard School of Engineering and Applied Sciences and the support of the Kavli Institute and Wyss Institute at Harvard University. J.S. acknowledges start-up funds from the University at Buffalo.

References

- ABAQUS. Reference Manual. ABAQUS Inc, Pawtucket, RI, 2010.
- Aberg, M., Gudmundson, P., 1997. The usage of standard finite element codes for computation of dispersion relations in materials with periodic microstructure. *J. Acoust. Soc. Am.* 102 (4), 2007–2013.
- Babae, S., Shim, J., Weaver, J.C., Chen, E.R., Patel, N., Bertoldi, K., 2013. 3d soft metamaterials with negative poisson's ratio. *Adv. Mater.* 25 (36), 5044–5049.
- Babae, S., Wang, P., Bertoldi, K. Three-dimensional adaptive soft phononic crystals, submitted for publication.
- Bathe, Klaus-Jrgen, 1996. *Finite Element Procedures*. Prentice Hall, Englewood Cliffs, N.J.
- Bertoldi, K., Boyce, M.C., 2008. Wave propagation and instabilities in monolithic and periodically structured elastomeric materials undergoing large deformations. *Phys. Rev. B* 78 (18).
- Bertoldi, K., Gei, M., 2011. Instabilities in multilayered soft dielectrics. *J. Mech. Phys. Solids* 59 (1), 18–42.
- Bertoldi, K., Boyce, M.C., Deschanel, S., Prange, S.M., Mullin, T., 2008. Mechanics of deformation-triggered pattern transformations and superelastic behavior in periodic elastomeric structures. *J. Mech. Phys. Solids* 56 (8), 2642–2668.
- Brillouin, L., 1946. *Wave Propagation in Periodic Structures*. McGraw-Hill.
- Casadei, F., Dozio, L., Ruzzene, M., Cunefare, K.A., 2010. Periodic shunted arrays for the control of noise radiation in an enclosure. *J. Sound Vib.* 329 (18), 3632–3646.
- Casadei, F., Beck, B.S., Cunefare, K.A., Ruzzene, M., 2012. Vibration control of plates through hybrid configurations of periodic piezoelectric shunts. *J. Intell. Mater. Syst. Struct.* 23 (10), 1169–1177.
- Cheng, W., Wang, J.J., Jonas, U., Fytas, G., Stefanou, N., 2006. Observation and tuning of hypersonic bandgaps in colloidal crystals. *Nat. Mater.* 5 (10), 830–836.
- Danielsson, M., Parks, D.M., Boyce, M.C., 2002. Three-dimensional micromechanical modeling of voided polymeric materials. *J. Mech. Phys. Solids* 50 (2), 351–379.
- Geymonat, G., Muller, S., Triantafyllidis, N., 1993. Homogenization of nonlinearly elastic-materials, microscopic bifurcation and macroscopic loss of rank-one convexity. *Arch. Ration. Mech. Anal.* 122 (3), 231–290.
- Holzappel, Gerhard A., 2000. *Nonlinear Solid Mechanics: A Continuum Approach for Engineering*. Wiley, Chichester; New York.
- Hussein, M.I., 2009. Theory of damped Bloch waves in elastic media. *Phys. Rev. B* 80, 212301.
- Jensen, J.S., 2003. Phononic band gaps and vibrations in one- and two-dimensional mass-spring structures. *J. Sound Vib.* 266 (5), 1053–1078.
- Jim, K.L., Leung, C.W., Lau, S.T., Choy, S.H., Chan, H.L.W., 2009. Thermal tuning of phononic bandstructure in ferroelectric ceramic/epoxy phononic crystal. *Appl. Phys. Lett.* 94 (19).
- Kang, S.H., Shan, S., Komrlj, A., Noorduyn, W.L., Shian, S., Weaver, J.C., Clarke, D.R., Bertoldi, K., 2014. Complex ordered patterns in mechanical instability induced geometrically frustrated triangular cellular structures. *Phys. Rev. Lett.* 112, 098701.
- Kittel, Charles, 2005. *Introduction to Solid State Physics*, Wiley, Hoboken, NJ.
- Kushwaha, M.S., Halevi, P., Dobrzynski, L., Djafarirouhani, B., 1993. Acoustic band-structure of periodic elastic composites. *Phys. Rev. Lett.* 71 (13), 2022–2025.
- Lakes, R., 2001. Elastic and viscoelastic behavior of chiral materials. *Int. J. Mech. Sci.* 43 (7), 1579–1589.
- Liu, Y.Z., Yu, D.L., Zhao, H.G., Wen, J.H., Wen, X.S., 2008. Theoretical study of two-dimensional phononic crystals with viscoelasticity based on fractional derivative models. *J. Phys. D – Appl. Phys.* 41, 065503.
- Liu, Z.Y., Chan, C.T., Sheng, P., 2002. Three-component elastic wave band-gap material. *Phys. Rev. B* 65 (16).
- Maldovan, Martin, Thomas, Edwin L., 2009. *Periodic Materials and Interference Lithography for Photonics, Phononics and Mechanics*. Wiley-VCH, Weinheim.
- Marsden, Jerrold E., Hughes, Thomas J.R., 1983. *Mathematical Foundations of Elasticity*. Prentice-Hall Civil Engineering and Engineering Mechanics Series. Prentice-Hall, Englewood Cliffs, N.J.
- Martinsson, P.G., Movchan, A.B., 2003. Vibrations of lattice structures and phononic band gaps. *Quart. J. Mech. Appl. Math.* 56, 45–64.
- Movchan, A.B., Movchan, N.V., Haq, S., 2006. Localised vibration modes and stop bands for continuous and discrete periodic structures. *Mater. Sci. Eng. A–Struct. Mater. Properties Microstruct. Process.* 431 (1–2), 175–183.
- Psarobas, I.E., 2001. Viscoelastic response of sonic band-gap materials. *Phys. Rev. B* 64, 012303.
- Shim, J., Perdigou, C., Chen, E.R., Bertoldi, K., Reis, P.M., 2012. Buckling-induced encapsulation of structured elastic shells under pressure. *Proc. Natl. Acad. Sci. USA* 109 (16), 5978–5983.
- Shim, J., Shan, S.C., Komrlj, A., Kang, S.H., Chen, E.R., Weaver, J.C., Bertoldi, K., 2013. Harnessing instabilities for design of soft reconfigurable auxetic/chiral materials. *Soft Matter* 9 (34), 8198–8202.
- Spadoni, A., Ruzzene, M., Gonella, S., Scarpa, F., 2009. Phononic properties of hexagonal chiral lattices. *Wave Motion* 46 (7), 435–450.
- Su, X.X., Wang, Y.F., Wang, Y.S., 2012. Effects of poisson's ratio on the band gaps and defect states in two-dimensional vacuum/solid porous phononic crystals. *Ultrasonics* 52 (2), 255–265.
- Triantafyllidis, N., Maker, B.N., 1985. On the comparison between microscopic and macroscopic instability mechanisms in a class of fiber-reinforced composites. *J. Appl. Mech.–Trans. ASME* 52 (4), 794–800.
- Vasseur, J.O., Djafarirouhani, B., Dobrzynski, L., Kushwaha, M.S., Halevi, P., 1994. Complete acoustic band-gaps in periodic fiber-reinforced composite-materials – the carbon-epoxy composite and some metallic systems. *J. Phys.–Condens. Matter* 6 (42), 8759–8770.
- Vasseur, J.O., Hladky-Hennion, A.C., Djafari-Rouhani, B., Duval, F., Dubus, B., Pennec, Y., Deymier, P.A., 2007. Waveguiding in two-dimensional piezoelectric phononic crystal plates. *J. Appl. Phys.* 101 (11).
- Wang, L.F., Bertoldi, K., 2012. Mechanically tunable phononic band gaps in three-dimensional periodic elastomeric structures. *Int. J. Solids Struct.* 49 (19–20), 2881–2885.
- Wang, P., Shim, J.M., Bertoldi, K., 2013. Effects of geometric and material nonlinearities on tunable band gaps and low-frequency directionality of phononic crystals. *Phys. Rev. B* 88 (1).
- Wu, T.T., Huang, Z.G., Lin, S., 2004. Surface and bulk acoustic waves in two-dimensional phononic crystal consisting of materials with general anisotropy. *Phys. Rev. B* 69 (9).
- Yeoh, O.H., 1993. Some forms of the strain-energy function for rubber. *Rubber Chem. Technol.* 66 (5), 754–771.
- Zalpaev, V.V., Movchan, A.B., Poulton, C.G., McPhedran, R.C., 2002. Elastic waves and homogenization in oblique periodic structures. *Proc. Roy. Soc. A – Math. Phys. Eng. Sci.* 458 (2024), 1887–1912.
- Zhou, X.Z., Wang, Y.S., Zhang, C.Z., 2009. Effects of material parameters on elastic band gaps of two-dimensional solid phononic crystals. *J. Appl. Phys.* 106 (1).